

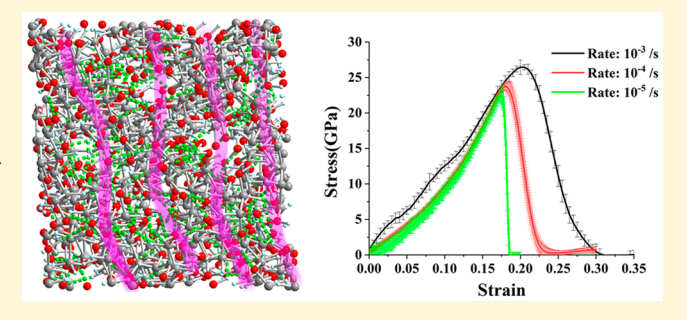
Crystalline Cellulose under Pyrolysis Conditions: The Structure— **Property Evolution via Reactive Molecular Dynamics Simulations**

Qi Qiao, Xiaobao Li, and Liangliang Huang*,

[†]School of Chemical, Biological & Materials Engineering, University of Oklahoma, Norman, Oklahoma 73019, United States *College of Chemical Engineering, Nanjing Forestry University, Nanjing 210037, P. R. China

Supporting Information

ABSTRACT: As a primary component of cell walls of plants, algae, bacteria, and other natural biomaterials, cellulose has attracted research attention and is the key to effective conversion of natural biomaterial into processable advanced functional materials. From the chemistry point of view, a typical crystalline cellulose is composed of linear chains of hundreds of β -1,4-linker glucose units. Therefore, inter and intra hydrogen bonding interactions play a decisive role of the structure-property relationship of cellulose based materials. Despite research progress from past decades, the fundamental mechanism of how cellulose structure transforms under



pyrolysis conditions and the practical guideline of how cellulose properties are fined tuned accordingly are still incomplete. In this work, a series of reactive molecular dynamics calculations has been designed to reveal the structural evolution of crystalline cellulose under pyrolysis treatments. Through the detailed analysis of cellulose configuration change, hydrogen bonding network variation, reaction and redistribution of carbon, oxygen and hydrogen elements, and Young's modulus, a molecule level insight of crystalline cellulose and its structural evolution under pyrolysis conditions has been constructed via reactive molecular dynamics simulations. We anticipate those theoretical results could effectively promote the design, the manufacture, and the optimization of cellulose based materials for relevant emerging applications.

1. INTRODUCTION

Cellulose exists in algae, bacteria, and other natural biomaterials as a basic building block. It is also a primary component of cell walls of green plants, along with hemicellulose and lignin. Cellulose based materials have been widely used in many applications, for example, biofuel productions,^{1,2} paper manufactory,^{3,4} construction industry,^{5–7} energy related fields,^{8–11} drug delivery,^{12–17} and biomedical therapy,^{18–20} to just name a few. The unique properties of nontoxicity, good biocompatibility, high biodegradability, high water adsorption, and great mechanical properties make cellulose one of the most promising candidates to address the increasing challenges in environmental, ecological, and energy fields.

Chemically, cellulose is a polysaccharide that consists of a linear chain of thousands of repeating D-glucose units, which are interlinked with β -1,4-linkages. Hydroxyl groups of cellulose chains and the inter/intra hydrogen bonding (HB) networks are dominating structural factors to cellulose properties. The utilization of cellulose based materials largely depends on the effective manipulation of cellulose HB networks. Accordingly, various treatments have been proposed to process raw cellulose materials, which could be classified as the following categories: (1) mechanical treatments such as milling, ^{21,22} grinding/refining, ^{23–25} high-pressure homogenizers, ^{26–29} cryocrushing, ^{27,30,31} and high intensity ultrasonic treatments; 32-34 (2) hydrolysis treatments 35-56 via the application of dilute acid, concentrated acid, enzyme, or autohydrolysis; (3) pyrolysis treatments⁵⁷⁻⁶¹ through the steam, hydrothermolysis, or wet oxidation; (4) chemical treatments 32,42,62-69 from oxidizing agents, alkali, acid, and organic solvents; (5) electrical, biological, and other treatments. 70-79

Most recently, producing cellulose based advanced materials via subtle treatment strategies has been brought to a new horizon. Exciting progresses include the milestone work of Hu⁶² and co-workers where they processed natural wood chemically to remove lignin, followed by a mechanical compressing to fine-tune the remaining cellulose structures into crumple and interlock. The transformed wood, mostly composed of structurally manipulated cellulose, is mechanically more than 10 times stronger than steel. 62 Selectively removing hemicellulose and lignin has witnessed other promising progresses, including compressible carbon sponges and high surface area activated carbon for chemical and biosensor development and water/oil separations. 63,80-83 Making use of

Special Issue: Proceedings of PPEPPD 2019

Received: July 17, 2019 Accepted: October 4, 2019 Published: October 17, 2019 the inherent structural and chemical properties is key to producing cellulose based advanced materials and maximizing their performance. It is worth noting that available results seem to suggest that having a proper amount of lignin is beneficial. The hypothesis is that the leftover lignin helps to bind cellulose fibers when further processed.

On the other hand, despite the importance and recent promising progress of the field, the theoretical understanding of cellulose based materials and their fundamental structureproperty relationship are still far from complete. There is a pressing need to develop molecule level understandings of cellulose based materials and how their structure and property evolve under various treatments. To date, the majority of theoretical research efforts are from ab initio density functional theory (DFT) and classical force field based molecular dynamics (MD) simulations of crystalline cellulose structures and corresponding electronic properties.^{84–89} The breakdown of cellulose under solution (such as water, acid, or ionic liquid environments) or pyrolysis conditions has also been studied computationally. For example, classical MD simulations were used to simulate the surface of cellulose I β and its interactions with water. 90 Matthews and co-workers used molecular mechanics (MM) simulations to study the crystalline cellulose configuration changes with surrounding water. 91 They found that the cellulose unit was expanded and twisted and that the formation of an adjacent water layer on the cellulose surface might delay the transitions of enzymes and further result in a slower hydrolysis rate in the enzyme-catalyzed hydrolysis approach. 91 They also found 92 that the twisting between cellulose chains results in the formation of a 3D hydrogen bond network inside hydrate cellulose I β microfibrils under high temperature (~500 K). Ab initio and MD simulations have also been used to understand the dissolution mechanism of cellulose in aqueous solutions. Janesko et al. 93 applied DFT calculations to study the interaction between cellulose and charged ions in ionic liquids (ILs). Payal and co-workers⁹² carried out ab initio molecular dynamics (AIMD) simulations to study the dissolution of cellulose I β monomers in ILs. They found that the breaking of the hydrogen bond network was the key factor for cellulose dissolution. Similarly, Liu et al. 55 found in their MD simulations that the strong hydrogen bonding between anion and cellobiose could significantly impact cellulose dissolution. Moreover, other researchers have also reported that the changes of interchain and intrachain hydrogen bond network lead to cellulose dissolution in ILs. When it comes to pyrolysis treatments, Bergenstråhle et al. 99

reported via classical MD simulations that cellulose I β crystal changed its structure when the temperature was above 450 K. Assary et al.¹⁰⁰ and Mayes et al.¹⁰¹ performed DFT calculations to study the fast pyrolysis of cellulose. They both observed cellobiose depolymerization, epoxide formation, and the production of levoglucosan (LGA). Agarwal et al. 102 performed both AIMD and Car-Parrinello molecular dynamics (CPMD) simulations to study cellulose decomposition pathways. They found that the cellulose decomposition to liquid intermediates started around 260 °C and LGA was produced from the fast pyrolysis between 400 and 600 °C, agreeing well with the results of Assary and Mayes. The authors also used classical MD to simulate the IR of cellulose I β crystal at 300-500 K. ¹⁰³ The IR agreed with that of experiments, and high temperatures can weaken cellulose intrachain hydrogen bonds, eventually leading to the formation of a 3-D hydrogen bonding network.

In recent years, reactive force field (ReaxFF) based MD simulation (RxMD) has gained more and more attention from the cellulose research community. It is mainly due to the advantages that electronic/reaction details and large time/ space scale computations can be achieved simultaneously in RxMD simulations. A number of RxMD simulations have been reported for cellulose, hemicellulose, lignin, and their mixtures. For example, Beste and co-workers 104 reported a RxMD study of the conversion of lignin at various temperatures, and they found that the 5-5 linkage was the weakest linker during the cyclization and dehydrogenation. Zheng and co-workers 105 studied the pyrolysis process of amorphous cellulose at temperatures from 500 to 1400 K. The reported pyrolysis products agree well with available experiments, which also confirms that the applied ReaxFF force field provides an accurate description of cellulose pyrolysis processes. Meanwhile, Paajanen et al. 106 studied the amorphous cellulose decomposition from 1400 to 2000 K. They observed that the breaking of $1-4-\beta$ bonds eventually leads to the cellulose decomposition and that the decomposition products are mainly glycolaldehyde, water, formaldehyde, and formic acid, which agreed with experimental results.

In this work, a series of RxMD simulations have been performed to reveal the structural evolution of crystalline cellulose I β via pyrolysis treatments under isolated conditions. By varying the pyrolysis temperature, the change of cellulose crystallinity, the variation of inter/intra HB networks, and the reaction and distribution of C, O, and H elements have been recorded and analyzed. In addition, the pyrolysis treated cellulose and its mechanical properties were also discussed in terms of Young's modulus and the yield tensile stress. Despite that the pyrolysis process was modeled under isolated conditions, that is, no contribution was considered from oxygen and water of the air, this work demonstrates a general computational protocol to study cellulose systems under reactive conditions. Furthermore, the constructed structureproperty relationship could shed light on how to select pyrolysis conditions and achieve desirable structural, chemical, and mechanical properties of engineered cellulose based materials. This Article is organized as following: Section 2 presents a brief introduction to the ReaxFF reactive force field, a simulation protocol, and a list of computational characterizations. Section 3 contains the calculation results and discussion of structural evolution of crystalline cellulose I β as a function of time, the characterizations of inter/intra HB networks, and the mechanical properties of processed cellulose. Conclusions are finally provided in section 4.

2. MODEL AND SIMULATION DETAILS

2.1. Crystalline Cellulose. The initial cellulose I β crystal was generated by the cellulose builder from Gomes and coworkers, 107,108 with the lattice parameters 108 of 7.784 Å, 8.201 Å, 10.380 Å, 90°, 90°, and 96.550° from experimental XRD and neutron fiber diffraction results at 293 K. In our RxMD simulations, a 2 × 2 × 6 supercell was constructed which produces a triclinic simulation box of 15.568 × 16.402 × 62.280 ų. In this work, benchmark calculations on larger systems have been performed at the initial stage of this research. Quantitively similar results were obtained about properties such as the hydrogen bonding network and the Young's modulus. Also, we followed the choice of simulation box size and used a similar total number of atoms in the cellulose model. 105,106,109,110 Figure 1a shows characteristic

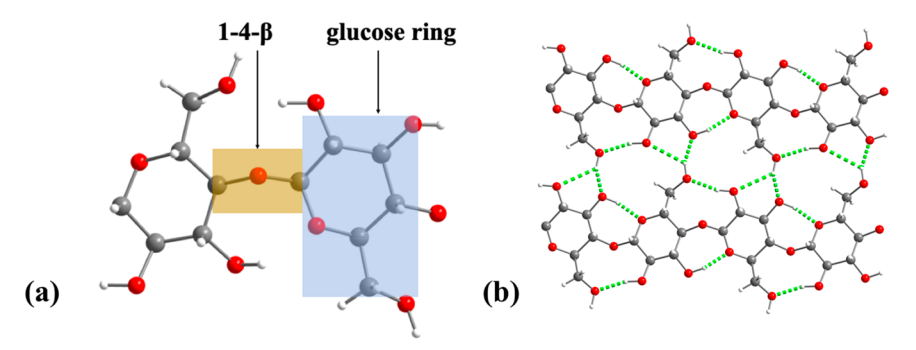


Figure 1. Initial configurations of the $I\beta$ crystalline cellulose: (a) two characteristic covalent bonds in a single cellulose chain; (b) the hydrogen bonding network from two parallel cellulose chains.

covalent bonds of crystalline cellulose, namely, the bonds of the glucose unit that hold the ring structure and the $1-4-\beta$ bonds that connect glucose units. It is expected that, at elevated temperatures, either the glucose ring structure or the $1-4-\beta$ bond would break down. Besides covalent bonds, the HB networking is also critical to cellulose properties. As shown in Figure 1b, hydrogen bonds (green dashed lines) come from both inter and intra cellulose chains. As the temperature increases, the crystallinity of the cellulose structure decreases, consequently producing a change of the inter and intra HB networks, which significantly affects the mechanical properties of the pyrolysis treated cellulose.

2.2. ReaxFF Reactive Force Field and RxMD Simulation. Proposed by van Duin and co-workers in 2001, the ReaxFF reactive force field has been actively developed to describe complex and large-scale reactive systems, which could contain hundreds to several thousands of atoms. 111 So far, ReaxFF has been applied to describe complex systems such as protein/DNA, 112,113 membrane fuel cell systems, 114 and very complicated coal structure and properties. 115 ReaxFF has become a choice for multiscale modeling of systems with adsorption, dissociation, and complicated reactions. 116-118 Unlike traditional definitions of bonds, angles, and dihedrals of classical force fields, a concept of bond order 119-123 has been developed in ReaxFF to calculate atomic connections and system energies in order to describe the continuous bond formation and breaking and mimic the reaction pathway in the systems. 111 These advantages make ReaxFF a useful tool in predicting structural evolution, tracing intermediates, and analyzing final products. Recently, ReaxFF has been successfully used for the study of the mechanism of the pyrolysis process of cellulose, hemicellulose, lignin, and their derivatives. 104-106,109,126,127 Generally speaking, ReaxFF is 1 order slower than the nonreactive force fields; the most expensive calculations part of ReaxFF have been the charge calculations that come from the electronegativity equalization method (EEM) by Mortier and co-workers. 128-130 However, with the help of parallel calculations, a time scale of microseconds trajectory could be archived. 117 More details of ReaxFF are available from recent reviews. 131-133 The ReaxFF parameters used in this work have successfully described cellulose systems. 106,109

All RxMD simulations were performed by the LAMMPS package. The isothermal–isobaric (NPT) ensemble was applied where the pressure was maintained at 1 atm. The temperature was controlled via the temperature-programmed protocol, changing from 300 K slowly to targeted final temperatures (500, 800, 1000, 1100, 1200, and 1300 K).

The Berendsen method with a temperature damping coefficient of 100 fs was applied to maintain the system temperature. Initial velocity was assigned according to the Boltzmann distribution. A time step of 0.25 fs was adopted in all calculations. Each of the RxMD simulations in this work has a trajectory of at least 10 ns. For the cellulose decomposition distribution analysis, longer simulations have been performed for 60 ns for 1200 and 1300 K. For the Young's modulus analysis, after the 10 ns trajectory, an additional calculation of 1 ns was carried out to collect the data at a smaller time step (0.05 fs). Other calculations were performed at a time step of 0.25 fs. It is worth noting that identifying the true equilibrium state is always important and challenging for molecule simulations. Technically, the equilibrium state is justified via various analyses such as the total energy of the system, the root-mean-square deviation of atomic positions, diffusion coefficients, etc. Zheng and co-workers have summarized that cellulose is thermally stable in the temperature ranges of 673-1073 K (experimentally) and 500-1400 K (computationally). The wide temperature range is mainly due to different cellulose resources and the treatment conditions (isolated, vacuum, with a mixture of gases or liquids). Our work shows that cellulose is generally stable up to 1000 K, which qualitatively agrees with other computational studies. In addition, we have tested the calculations for different time scales, from 25 ns up to 100 ns. No qualitative difference was observed. However, it is worth noting that the choice of simulation time depends critically on the property of interest; for example, to gain cellulose dissociation kinetics, longer calculations are recommended.

2.3. Monitored Properties from RxMD Simulation. 2.3.a. Hydrogen Bonding Network. The HB networking has been widely used to describe structural changes of crystalline cellulose $I\beta$ and is considered as a packing indicator when linear cellulose chains roll into highly ordered structures. In this work, the HB criteria proposed by Nishiyama and co-workers were adopted

$$R_{\rm L}^{\rm O\cdots H} < R^{\rm O\cdots H} < R_{\rm H}^{\rm O\cdots H}; ~~\theta^{\rm O\cdots HO} < \theta_{\rm C}^{\rm O\cdots HO}$$

where $R^{\text{O}\cdots\text{H}}$ is the distance between the HB acceptor (O) and the HB donor (H). The low and high thresholds are 1.7 and 2.6 Å, respectively. $\theta^{\text{O}\cdots\text{HO}}$ represents the angle O···O–H for the HB formation where the threshold angle is 110° .

2.3.b. Computational X-ray Diffraction. X-ray diffraction (XRD) patterns are sensitive to spacings between layers or rows of atoms and are capable of determining the orientation of a single crystal or grain. XRD has been utilized to identify crystal structures and measure the size, shape, and internal

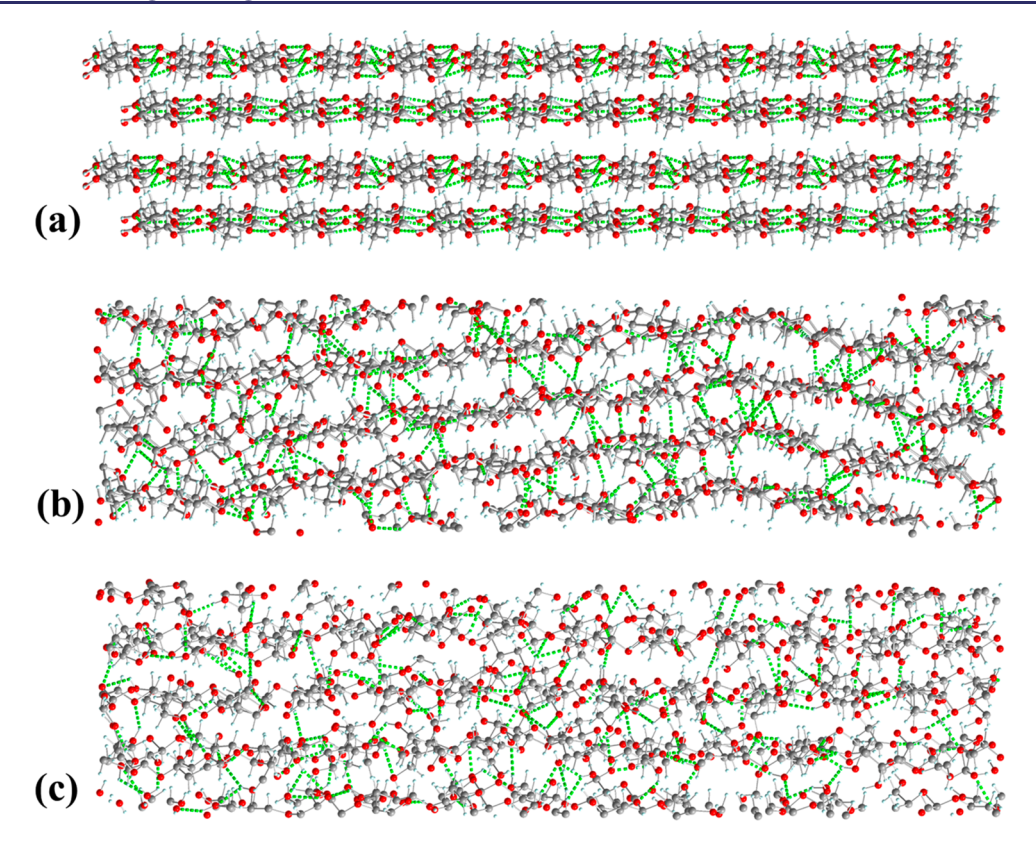


Figure 2. Cellulose configuration changes at different temperatures: (a) initial cellulose crystalline structure (exp. 293 K); ¹⁰⁸ (b) cellulose structure at 300 K; (c) intermediate cellulose structure at 1100 K. When the temperature is higher than 1200 K, the cellulose structure will decompose. The hydrogen bonding network is shown in green dashed lines.

stress of small crystalline regions. It is also a primary tool for determination of nanocrystallite orientation in polymers. In this work, XRD plots were calculated to monitor the structural evolution of crystalline cellulose: the peak positions are determined by the lattice parameters, while the peak intensities are from the motif. XRD calculations were carried out by the Mercury and Diamond software; more information is available from the software manual. 139,140

2.3.c. Young's Modulus. Young's modulus defines the relationship between stress (force per unit area) and strain (proportional deformation) in the linear elasticity regime of a uniaxial deformation. 141 A larger Young's modulus suggests a better stiffness of a material. Young's modulus could be experimentally determined via X-ray diffraction 142 or Raman spectroscopy. 143 Computationally, several methods have been proposed to calculate this elastic modulus. 143–146 One method is to enlarge the simulation box length repeatedly by a small amount, along the axis where the stress is applied. The simulation system is then reoptimized at each new fixed cell unit. 110,146 Another method is to allow the simulation box to elongate continuously at a defined strain rate for a uniaxial tensile deformation. Several articles have adopted the second method to estimate the Young's modulus for amorphous polymers and metals. 147-152

This work also uses the second method to monitor the uniaxial tensile deformation at three different strain rates. In those simulations, the tensile stress is the negative value of pressure along the corresponding direction. The strain is then calculated by the amount of the length change for that direction. Young's modulus (E) is the ratio of tensile stress $(\sigma(\varepsilon))$ and strain ε , $E = \sigma(\varepsilon)/\varepsilon$. From the stress—strain

diagram, the point of yielding is estimated by the offset yield method, also known as 0.2% offset yield strength. As shown in the following section, the yield strength is obtained by drawing through the point of the horizontal axis of $\varepsilon=0.2\%$, a line parallel to the initial straight-line portion of the stress—strain diagram.

3. RESULTS AND DISCUSSION

3.1. Cellulose Configuration under Different Temperatures. As shown in Figure 2, the temperature effect on cellulose configuration has been monitored. Figure 2a displays the final configurations from different temperatures, whereas the hydrogen bonding network of cellulose chains is illustrated by green dashed lines. In Figure 2b and c, the cellulose has been treated at 300 and 1100 K, respectively. The structure gets corrugated and twisted due to the pyrolysis process, which in turn could modify the hydrogen bonding network. Both traditional and ReaxFF force fields provide similar descriptions to cellulose conformation and its hydrogen bonding network. We analyzed and compared the cellulose unit cell predicted from this work and reported experimental and computational data from the literature. Nishiyama and co-workers 108 reported atomistic coordinates of cellulose crystal via XRD and neturon fiber diffraction at room temperature (293 K), which is adopted as the starting structure in this work. Matthews and co-workers 91,92 used the CHARMM force field to discuss cellulose structures. Bergenstråhle⁹⁹ observed similar cellulose structural changes via the GROMOS, PCFF, MM3, and CHARMM force fields. In Table S1 of the Supporting Information, the equilibrium unit cell parameters are listed

from experiments and different computational studies, including this work.

Compared with results from traditional force fields, 89,92,99,153-155 ReaxFF described the cellulose structure similar to that of the experimental value at 293 K. 108 It is worth noting that the unit cell angle γ is smaller than the experimental result, which is probably due to the underestimation of cellulose chain—chain dispersion interactions via the ReaxFF force field. A smaller γ value is also reported from calculations with traditional force fields at 300 K. 92,99 In our calculations, when the temperature was increased to 500 K, larger unit cell parameters were observed, also similar to results from traditional force fields.⁹⁹ As discussed in the literature, 92,99 the change of unit cell shape (α and β angles) indicates the interchain sliding of cellulose crystal. When the temperature increased from 500 to 1100 K in this work, the unit cell change became more significant, suggesting the increasing distance between cellulose chains. Such a configurational change eventually leads to the structural collapse of cellulose at high temperatures, around 1100 K according to RxMD simulations in this work. In RxMD calculations, the cellulose structure was stable up to 1000 K. At 1100 K, cellulose was stable for a few nanoseconds, but then it gradually decomposed. Even though cellulose is not thermally stable at 1100 K, the observed stability transition is important. When the temperature was beyond 1200 K, the cellulose structure quickly decomposed. Reaction products such as H₂₁ CO, H2O, and very little CO2 were observed, as shown in the Supporting Information. These pyrolysis products were also reported by previous work. 105,109

3.2. XRD of Cellulose Structures. XRD is a useful method to identify crystalline, semicrystalline, and amorphous structures. Here we calculated XRD to qualitatively determine the crystalline phase of cellulose under pyrolysis conditions. Since the initial cellulose crystal was built up based on experimental XRD data, ¹⁰⁸ we used its XRD here to represent experimental XRD results from Nishiyama and co-workers. The green region represents the peak ranges of experimental XRD results that were reported by other authors. ^{156–158} The cellulose structures at 300, 1000, and 1100 K were used to study the structure phase change under different pyrolysis temperatures. As shown in Figure 3, cellulose structures at 300

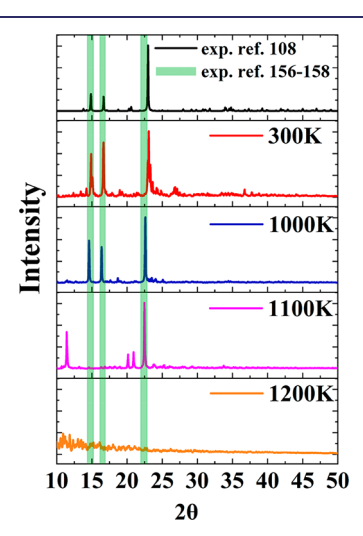


Figure 3. XRD of cellulose structures at different pyrolysis temperatures.

and 1000 K have similar XRD patterns as those of the experimental results (exp. 108), for both peak position and peak intensity. This suggests that I β crystalline cellulose has a relatively good thermal stability. When the temperature increases to 1100 K, there is a noticeable XRD peak shift when we calculate the XRD of the cellulose intermediate crystalline structure. From 300 to 1000 K, the calculations revealed cellulose structural changes, such as the corrugations and the twists of cellulose chains. However, the chains were generally still parallel to each other, and the distance between chains did not change too much. Therefore, no significant XRD peak shifting was observed between the initial crystalline cellulose and cellulose at temperatures from 300 to 1000 K. When the temperature was further increased to 1100 K, an obvious increase in cellulose chain-chain distance occurred. In addition, the twist of individual cellulose chains was more significant. Both contributed to the shift of XRD peaks from this temperature (1100 K) and up. It is also worth noting that the increased chain-chain distance reduced the total number of HBs between cellulose chains and eventually led to the collapse of cellulose structure. At 1200 K and above, XRD results showed an amorphous cellulose structure, suggesting the structural collapse at those higher pyrolysis temperatures.

3.3. Cellulose Decomposition and Element Distribution Analysis. Under pyrolysis temperatures of 1200 and 1300 K, the crystalline cellulose structure could fully decompose. The categories of pyrolysis products have already been studied, and one of the classifications 109 was adopted in this work: (a) organic gas composites which contain 1-4 carbon atoms; (b) light tar which contains 5-13 carbon atoms; (c) heavy tar which contains 14-39 carbon atoms; (d) char which contains more than 40 carbon atoms. As shown in Figure 4a, cellulose started to decompose into tar or heavy tar at the beginning of the simulations. After the crystalline structure was decomposed, several light tar products were detected, as well as light gas molecules such as CH₄ and CO. RxMD simulations with the same ReaxFF force field have been performed to understand the pyrolysis decomposition of cellulose, hemicellulose, and lignin. 105,106,109,159 From an experimental point of view, pyrolysis temperatures could be divided into the following ranges: 160 (1) 550-950 K (slow pyrolysis); (2) 850–1250 K (fast pyrolysis); (3) 1050–1300 K (flash pyrolysis). We adopted the concept and qualitatively treated temperatures from 500 to 800 K as slow pyrolysis, temperatures from 800 to 1000 K as medium pyrolysis, and temperatures of 1100 K and above as fast pyrolysis. It is also worth noting that cellulose pyrolysis at high temperatures has been investigated via the ReaxFF force field. 105,109 In this work, we mainly focus on cellulose structural evolution under low and medium pyrolysis temperatures. Cellulose decomposition products depend on the pyrolysis setting, that is, the initial cellulose structure (crystalline vs amorphous), the pyrolysis temperature (medium vs high), and the pyrolysis atmosphere (isolated vs ambient with CO₂, O₂, or H₂O). For the isolated condition and under a high temperature (>1200 K), we observed that cellulose should decompose completely into light products of H2, CO, H2O, and very little CO2 after a sufficiently long RxMD calculation (~60 ns).

From the materials perspective, it is desirable that the pyrolysis process only produces necessary changes to the structural and chemical properties of cellulose and maintains the maximum use of the elements of cellulose. If a large amount of gas-phase species, such as CO₂, CO, CH₄, H₂, and

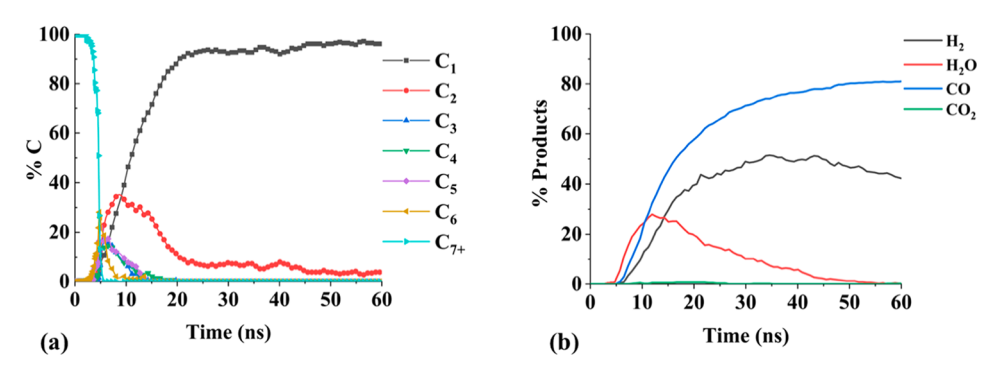


Figure 4. Analysis of cellulose decomposition at 1200 K: (a) The redistribution of carbon elements; C_1 , C_2 , ..., C_{7+} denote decomposition products having 1 carbon atom, 2 carbon atoms, ..., and 7 or more carbon atoms, respectively. (b) Light gas-phase molecules during the isolated pyrolysis process.

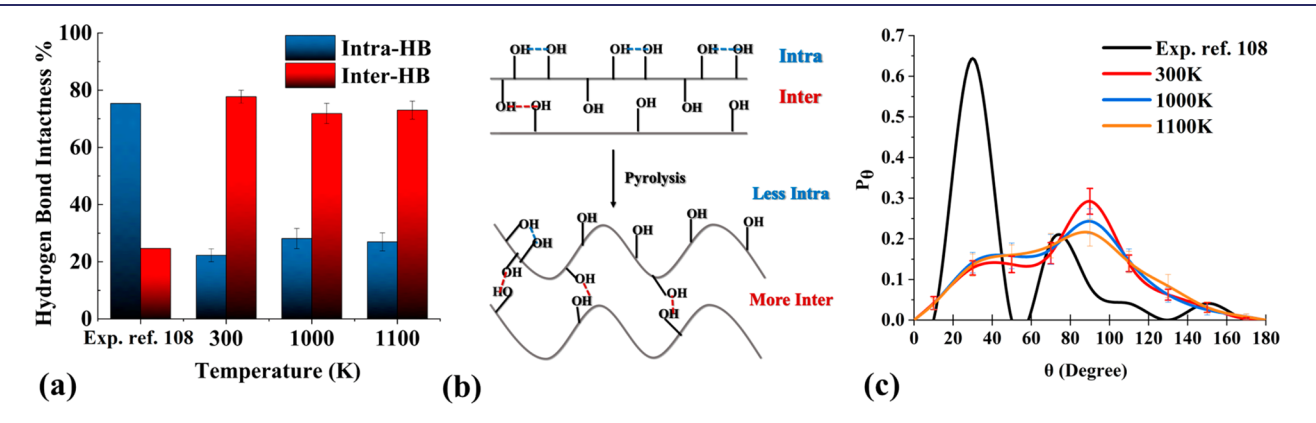


Figure 5. (a) The intrachain HB and interchain HB distributions at different pyrolysis temperatures. (b) A schematic illustration of the inter and intra HB network change due to pyrolysis temperature. (c) The HB angular distribution, which is through the analysis of the angle formed between the HB bond and the positive *Z* axis.

 $\rm H_2O$, is released during the pyrolysis process, the efficiency of converting cheap biomaterials to cellulose based advanced materials would be rather low. For the isolated pyrolysis conditions in this work, the calculations reveal that the release of $\rm CO_2$ is negligible, see Figure 4b, and that $\rm CO$ and $\rm H_2$ are the dominating gas-phase species. It is worth noting that gas-phase $\rm H_2O$ is released during the early stage of the pyrolysis process. At the studied high temperatures, the vapor water can further interact with cellulose and produce more $\rm CO$ and $\rm H_2$.

3.4. Cellulose Hydrogen Bonding Network. The cellulose configuration in Figure 2 shows that the corrugation and twist can lead the linear cellulose chains to a more complex three-dimensional hydrogen bonding network. To further monitor this change, the two types of hydrogen bonds have been distinguished, namely, the intrachain HBs that are formed between hydroxyl groups of same cellulose chains and the interchain HBs that are formed between hydroxyl groups from different cellulose chains. The percentage of hydrogen bond intactness is defined as the number of intra (or inter) HBs over the total number of HBs. Figure 5a shows the numerical analysis of the two hydrogen bonds where more interchain HBs exist under those studied pyrolysis conditions. For the pristine initial cellulose crystal, the majority is the intrachain HBs. In addition, comparing the initial model and cellulose at 300 and 1000 K, the total number of HBs is 292, 247 \pm 10, and 183 \pm 11, respectively. This indicates that the studied I β cellulose is thermally stable from 300 to 1000 K.

A scheme in Figure 5b illustrates the comparison of the hydrogen bonding network between the pristine $I\beta$ cellulose

crystal and the cellulose after the pyrolysis treatment. In the initial crystal state, all cellulose chains are linear and highly ordered, with most hydroxyl groups on a cellulose chain pointing to the same directions. As a result, forming intrachain HBs is easier than forming interchain HBs due to the structural hindrance. On the contrary, under pyrolysis treatments, the corrugation and twist of cellulose chains prevent the formation of intra HBs but promote those inter HBs. At finite temperatures, cellulose chains rotate, twist, and corrugate to form a three-dimensional hydrogen bonding (HB) network. Figure 5a reveals a significant difference between experiment (XRD and neutron fiber diffraction data) and RxMD simulations. This is likely due to the fact that, in RxMD simualtions, all hydrogen atoms are expressed explicitly. Their interactions contribute significantly to the HB network. However, XRD and neutron diffraction experiments cannot determine the exact locations of hydrogen atoms, which might lead to the incorrect description of the HB network. This explains the overestimated intra HB and the preferential HB angular distribution in Figure 5c: peak postions around 30, 70, and 150°. The HB angular distribution is through the analysis of the angle formed between the HB bond and the positive zaxis. In this work, the RxMD results show that inter HB bonds are critical to the 3D network. It is also the main reason why cellulose is stable even at high temperarures (for example, 1000 K in this work). The 3D HB network and its change due to temperature have been investigated also by classical force fields, with qualitatively similar results. 91,92,99,161 It is worth mentioning that the total number of hydrogen bonds should

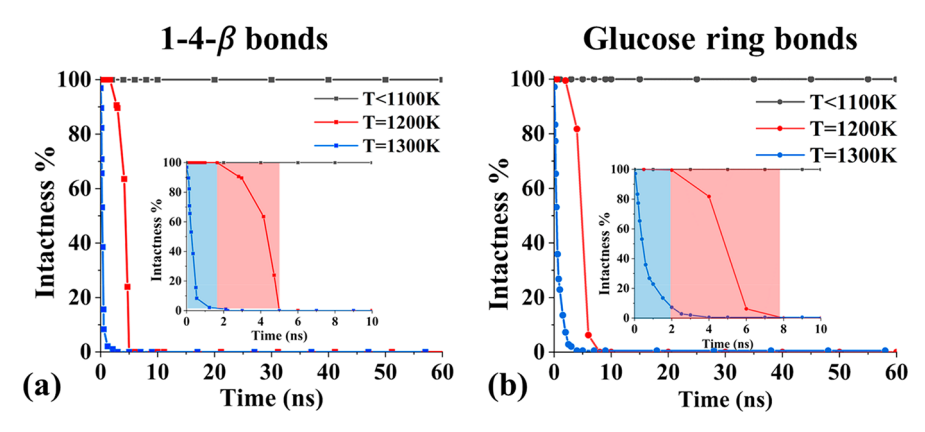


Figure 6. Intactness analysis of cellulose covalent bonds: (a) the $1-4-\beta$ bond; (b) the glucose ring. The red and blue regions respectively correspond to the time scales that $1-4-\beta$ bonds and glucose rings are detectable during the RxMD simulation.

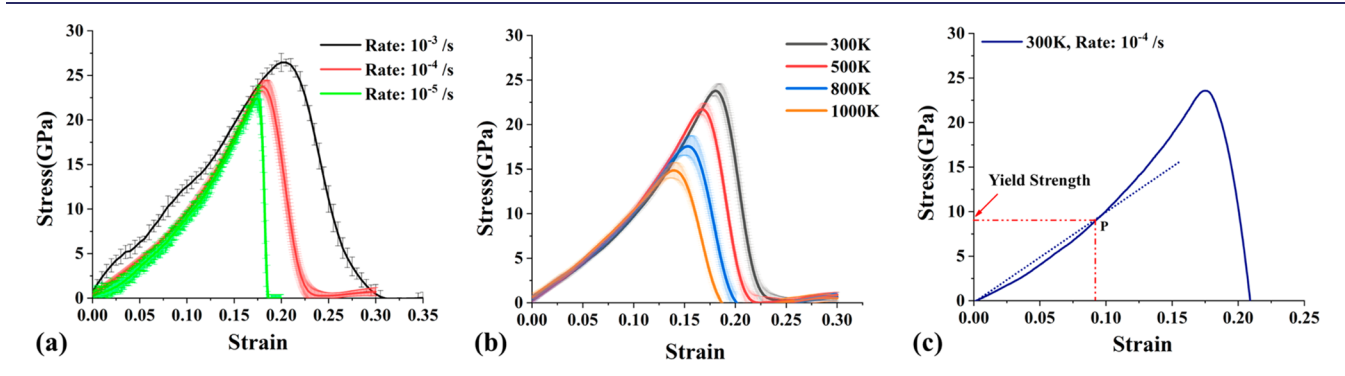


Figure 7. (a) The stress—strain diagram of cellulose at 300 K. The strain rate of $10^{-3}/s$ is in black, the strain rate of $10^{-4}/s$ is in red, and the strain rate of $10^{-5}/s$ is in green, respectively. (b) The stress—strain diagram of cellulose at 300, 500, 800, and 1000 K. The strain rate is kept at $10^{-4}/s$. (c) The determination of cellulose yield stress at the strain rate of $10^{-4}/s$ and 300 K.

decrease under even higher pyrolysis temperatures. This is because the distance between cellulose chains gets slightly enlarged under higher temperatures, and eventually those interchain HBs would disappear.

3.5. The Breakdown of Cellulose Structures. In order to gain the fundamental insight of when and how the cellulose structure breaks down, the two characteristic covalent bonds of Figure 1a have been monitored, and the definition of bond intactness is defined as follows: (1) for a 1-4- β bond, the oxygen atom remains connected with the exact same two carbon atoms during the pyrolysis process; (2) for the glucose ring structure, all bonds from the ring structure are monitored, as well as the C-OH and C-CH2OH groups that are connected with the ring structure. Each carbon in the glucose unit should remain bonded with the neighboring atoms during the pyrolysis process; in this work, the bond intactness is evaluated as a function of interatomic distance, to monitor the type, the breaking, and the formation of bonds via ReaxFF. 162 With the bond order information, the intactness of a molecule or structure is further evaluated to see whether and for how long atoms of the molecule/structure remain connected.

For the studied conditions, both $1-4-\beta$ and glucose ring bonds remain intact for the temperature range from 300 to 1000 K. When the temperature increased to 1200 K, $1-4-\beta$ bonds started to break down within 2 ns, and by the end of the 5 ns in the trajectory, all $1-4-\beta$ bonds were decomposed, as shown in the inset of Figure 6a. Meanwhile, the breakdown of glucose ring structures was also detected at 1200 K. Compared with the $1-4-\beta$ bond, the decomposition of the glucose ring was slightly delayed, and it took until 7.5 ns in the trajectory to

break all glucose rings. This suggests that the glucose ring is more thermally stable than the $1-4-\beta$ structure. At 1300 K, the breakdown was expedited: within 2 ns, all $1-4-\beta$ were decomposed, while the complete breakdown of glucose rings was achieved within 5 ns. However, no temperature range is identified where $1-4-\beta$ bonds are decomposed and the glucose rings remain intact. It is probably due to the dangling bonds of broken $1-4-\beta$ structures, which can further induce the breakdown of glucose rings. Under different conditions, that is, instead of isolated pyrolysis, with liquid or gas mediated pyrolysis processes, the $1-4-\beta$ bond breakdown does not spontaneously lead to the decomposition of glucose rings. Thus, the cellulose structure could be modified selectively, by removing only those $1-4-\beta$ bonds. It is also interesting to note the collective contributions from the 3-D HB network. At 1200 or 1300 K, where both $1-4-\beta$ bonds and cellulose rings were decomposing, the 3-D hydrogen bonding network was still able to hold together partial crystalline cellulose chains. It is worth pointing out that the dissociation energies for characteristic structural changes are 0.2-40 kcal/mol for the hydrogen bonded (HB) network, 51-76 kcal/mol for the glycosidic (1-4- β) bond cleavage, and 78–191 kcal/mol for the glucose ring dissociation. ^{163–165} In our calculations, when temperature was increasing from 300 K, the first structural change was from the 3-D HB network. At 1100 K, the thermo energy was able to further break down $1-4-\beta$ bonds and induce partial structural collapse of cellulose. In addition, the total number of HBs also decreased at 1100 K, which is more evidence of cellulose structural collapse. The simulation results also revealed that it is challenging to identify a temperature region where glucose

rings stay intact but the H-bonding network and $1-4-\beta$ bonds are broken. This is probably due to the fact that $1-4-\beta$ bonds and glucose rings alternate to form cellulose structures; see Figure 1. When $1-4-\beta$ bonds start to break down, the neighboring glucose rings become unsaturated and could easily interact with molecules or other parts of the partially collapsed cellulose. Between the covalent and HB bonds, is it possible to selectively remove the HB network and keep covalent bonds intact? More theoretical and experimental efforts are needed to validate the two hypotheses.

3.6. Young's Modulus Analysis. The configurational change of cellulose leads to the HB network variation, which inevitably affects cellulose mechanical properties. In this work, the uniaxial tensile deformation along the z direction has been calculated to evaluate the Young's modulus of cellulose. The deformation was carried out at 300 K at three different strain rates, namely, $10^{-3}/s$, $10^{-4}/s$, and $10^{-5}/s$. During the calculation, the stress (pressure) was only considered along the z direction and the pressure of the x and y directions was kept at zero. A time step of 0.05 fs was applied, and a total of 1 ns RxMD calculation was performed for each case. A smaller time step here was employed to avoid the error in calculating atom motions or any unstable structures. The Young's modulus was averaged using the data from the last 10% of the simulation trajectory. At 300 K, the calculated Young's modulus was about 113.24 \pm 3.85 GPa (see Figure 7a) at the strain rate of 10⁻⁴/s, which agreed well with other calculations. 110 From the literature, the Young's modulus of cellulose has been reported to be $(110-220) \pm 50$ GPa experimentally, ^{142,166-169} or in the range 110-173 GPa by computational studies. ^{99,110,143,144,146,153,155,170,171} The relatively small Young's modulus is probably coming from the adopted ReaxFF force field and the I β crystalline cellulose structure. In Figure 7b, we plotted the deformation curves for temperatures from 300 to 1000 K with a strain rate of $10^{-4}/s$. We observed a Young's modulus of 99.03 \pm 2.16, 95.67 \pm 3.65, and 94.34 \pm 3.08 GPa at 500, 800, and 1000 K, respectively. When the temperature increases, the Young's modulus decreases. This is because cellulose can deform easily at higher temperatures, leading to the drop of Young's modulus.

In addition, as shown in Figure 7c, at the strain rate of 10^{-4} /s, via the aforementioned proportional limit method, the yield stress was determined to be about 8.75 GPa, which is in excellent agreement with experimental and other modeling results. 110,172,173

4. CONCLUSION

While the classical force field has been adopted to study cellulose properties and cellulose interaction with other materials, chemical reaction and thermal decomposition of cellulose are beyond the reach. In this work, via ReaxFF based reactive molecular dynamics (RxMD) simulations, we observed bond breaking and structural change of cellulose at elevated temperatures. By changing the pyrolysis temperature from 300 to 1300 K, we are able to analyze the overall configuration, the covalent bonds of $1-4-\beta$ and glucose ring units, the inter and intra hydrogen bonding networks, and the element distributions systematically. XRD and Young's modulus have also been computed to compare with available experimental and previous modeling results. Key results include the following: (a) Cellulose is able to hold the general crystalline structure for temperatures up to 1000 K. The good

thermal stability is assisted by the interchange of inter- and intrachain HB networks. (b) When the pyrolysis temperature is beyond 1200 K, both 1-4- β bonds and glucose ring units will decompose. Light gas-phase molecules, such as CO and H_2 , are detected as major decomposition products. (c) Through the analysis of XRD, Young's modulus, and elements distribution, we show that the ReaxFF reactive force field is capable of describing both stable and dissociative properties of cellulose under isolated pyrolysis processes. Ultimately, this work provides an atomic level fundamental understanding of cellulose structural evolution via pyrolysis treatments. More studies of cellulose under real pyrolysis conditions, that is, instead of isolated conditions but via liquid or gas mediated pyrolysis processes, are worth pursuing. Moreover, the detailed mechanism of how cellulose, hemicellulose, and lignin respond differently to pyrolysis treatments could lead to a subtle manipulation and a successful conversion of biomass into advanced functional materials.

ASSOCIATED CONTENT

S Supporting Information

The Supporting Information is available free of charge on the ACS Publications website at DOI: 10.1021/acs.jced.9b00701.

(1) A table of comparison of unit cell parameters, angles between experiments, traditional force fields, and our models; (2) the configuration plots of 500, 800, 1000, and 1200 K; (3) the XRD plots of 500 and 800 K and element distribution of 1300 K; (4) the comparison of the stress—strain diagram for different strain rates at 300 K; (5) force field parameters we used in our work (PDF)

AUTHOR INFORMATION

Corresponding Author

*E-mail: hll@ou.edu.

ORCID

Liangliang Huang: 0000-0003-2358-9375

Notes

The authors declare no competing financial interest.

ACKNOWLEDGMENTS

It is a pleasure to acknowledge the discussion and advice from Dr. Xiawa (Eva) Wu, The Johns Hopkins University, about cellulose mechanical property calculations. Q.Q. and L.H. acknowledge the startup support from OU and partial support from the U.S. National Science Foundation (NSF) through grant CHE-1710102. We are very pleased to thank the OU Supercomputing Center for Education & Research (OSCER) at University of Oklahoma for their dedicated support.

REFERENCES

- (1) Rubin, E. M. Genomics of cellulosic biofuels. *Nature* **2008**, 454, 841.
- (2) Hill, J.; Nelson, E.; Tilman, D.; Polasky, S.; Tiffany, D. Environmental, economic, and energetic costs and benefits of biodiesel and ethanol biofuels. *Proc. Natl. Acad. Sci. U. S. A.* **2006**, 103 (30), 11206.
- (3) Nogi, M.; Kim, C.; Sugahara, T.; Inui, T.; Takahashi, T.; Suganuma, K. High thermal stability of optical transparency in cellulose nanofiber paper. *Appl. Phys. Lett.* **2013**, *102* (18), 181911.
- (4) Salajkova, M.; Valentini, L.; Zhou, Q.; Berglund, L. A. Tough nanopaper structures based on cellulose nanofibers and carbon nanotubes. *Compos. Sci. Technol.* **2013**, *87*, 103–110.

- (5) Sun, X.; Wu, Q.; Lee, S.; Qing, Y.; Wu, Y. Cellulose Nanofibers as a Modifier for Rheology, Curing and Mechanical Performance of Oil Well Cement. *Sci. Rep.* **2016**, *6*, 31654.
- (6) Li, F.; Mascheroni, E.; Piergiovanni, L. The Potential of NanoCellulose in the Packaging Field: A Review. *Packag. Technol. Sci.* **2015**, 28 (6), 475–508.
- (7) Juntaro, J.; Pommet, M.; Mantalaris, A.; Shaffer, M.; Bismarck, A. Nanocellulose enhanced interfaces in truly green unidirectional fibre reinforced composites. *Compos. Interfaces* **2007**, *14* (7–9), 753–762.
- (8) Thomas, B.; Raj, M. C.; B, A. K.; H, R. M.; Joy, J.; Moores, A.; Drisko, G. L.; Sanchez, C. Nanocellulose, a Versatile Green Platform: From Biosources to Materials and Their Applications. *Chem. Rev.* **2018**, *118* (24), *11575*–11625.
- (9) Zhu, H.; Luo, W.; Ciesielski, P. N.; Fang, Z.; Zhu, J. Y.; Henriksson, G.; Himmel, M. E.; Hu, L. Wood-Derived Materials for Green Electronics, Biological Devices, and Energy Applications. *Chem. Rev.* **2016**, *116* (16), 9305–9374.
- (10) Muhd Julkapli, N.; Bagheri, S. Nanocellulose as a green and sustainable emerging material in energy applications: a review. *Polym. Adv. Technol.* **2017**, 28 (12), 1583–1594.
- (11) Chen, H.; Ling, M.; Hencz, L.; Ling, H. Y.; Li, G.; Lin, Z.; Liu, G.; Zhang, S. Exploring Chemical, Mechanical, and Electrical Functionalities of Binders for Advanced Energy-Storage Devices. *Chem. Rev.* **2018**, *118* (18), 8936–8982.
- (12) Jacob, J.; Haponiuk, J. T.; Thomas, S.; Gopi, S. Biopolymer based nanomaterials in drug delivery systems: A review. *Mater. Today Chem.* **2018**, *9*, 43–55.
- (13) Löbmann, K.; Svagan, A. J. Cellulose nanofibers as excipient for the delivery of poorly soluble drugs. *Int. J. Pharm.* **2017**, *533* (1), 285–297.
- (14) Chin, S. F.; Jimmy, F. B.; Pang, S. C. Size controlled fabrication of cellulose nanoparticles for drug delivery applications. *J. Drug Delivery Sci. Technol.* **2018**, 43, 262–266.
- (15) Treesuppharat, W.; Rojanapanthu, P.; Siangsanoh, C.; Manuspiya, H.; Ummartyotin, S. Synthesis and characterization of bacterial cellulose and gelatin-based hydrogel composites for drugdelivery systems. *Biotechnol. Rep.* **2017**, *15*, 84–91.
- (16) Luo, H.; Ao, H.; Li, G.; Li, W.; Xiong, G.; Zhu, Y.; Wan, Y. Bacterial cellulose/graphene oxide nanocomposite as a novel drug delivery system. *Curr. Appl. Phys.* **2017**, *17* (2), 249–254.
- (17) Abo-Elseoud, W. S.; Hassan, M. L.; Sabaa, M. W.; Basha, M.; Hassan, E. A.; Fadel, S. M. Chitosan nanoparticles/cellulose nanocrystals nanocomposites as a carrier system for the controlled release of repaglinide. *Int. J. Biol. Macromol.* **2018**, *111*, 604–613.
- (18) Rahimi, M.; Shojaei, S.; Safa, K. D.; Ghasemi, Z.; Salehi, R.; Yousefi, B.; Shafiei-Irannejad, V. Biocompatible magnetic tris(2-aminoethyl)amine functionalized nanocrystalline cellulose as a novel nanocarrier for anticancer drug delivery of methotrexate. *New J. Chem.* **2017**, *41* (5), 2160–2168.
- (19) Madhusudana Rao, K.; Kumar, A.; Han, S. S. Polysaccharide based bionanocomposite hydrogels reinforced with cellulose nanocrystals: Drug release and biocompatibility analyses. *Int. J. Biol. Macromol.* **2017**, *101*, 165–171.
- (20) Sheikhi, A.; Hayashi, J.; Eichenbaum, J.; Gutin, M.; Kuntjoro, N.; Khorsandi, D.; Khademhosseini, A. Recent advances in nanoengineering cellulose for cargo delivery. *J. Controlled Release* **2019**, 294, 53–76.
- (21) Sun, Y.; Cheng, J. Hydrolysis of lignocellulosic materials for ethanol production: a review. *Bioresour. Technol.* **2002**, 83 (1), 1–11.
- (22) Millett, M. A.; Baker, A. J.; Satter, L. D. Physical and chemical pretreatments for enhancing cellulose saccharification. *Biotechnol. Bioeng. Symp.* **1976**, No. 6, 125–153.
- (23) Iwamoto, S.; Nakagaito, A. N.; Yano, H. Nano-fibrillation of pulp fibers for the processing of transparent nanocomposites. *Appl. Phys. A: Mater. Sci. Process.* **2007**, *89* (2), 461–466.
- (24) Bandera, D.; Sapkota, J.; Josset, S.; Weder, C.; Tingaut, P.; Gao, X.; Foster, E. J.; Zimmermann, T. Influence of mechanical treatments on the properties of cellulose nanofibers isolated from microcrystal-line cellulose. *React. Funct. Polym.* **2014**, *85*, 134–141.

- (25) Panthapulakkal, S.; Sain, M. Preparation and Characterization of Cellulose Nanofibril Films from Wood Fibre and Their Thermoplastic Polycarbonate Composites. *Int. J. Polym. Sci.* **2012**, 2012, 381342.
- (26) Zimmermann, T.; Bordeanu, N.; Strub, E. Properties of nanofibrillated cellulose from different raw materials and its reinforcement potential. *Carbohydr. Polym.* **2010**, 79 (4), 1086–1093.
- (27) Dufresne, A.; Cavaillé, J.-Y.; Vignon, M. R. Mechanical behavior of sheets prepared from sugar beet cellulose microfibrils. *J. Appl. Polym. Sci.* **1997**, *64* (6), 1185–1194.
- (28) Stelte, W.; Sanadi, A. R. Preparation and Characterization of Cellulose Nanofibers from Two Commercial Hardwood and Softwood Pulps. *Ind. Eng. Chem. Res.* **2009**, *48* (24), 11211–11219.
- (29) Leitner, J.; Hinterstoisser, B.; Wastyn, M.; Keckes, J.; Gindl, W. Sugar beet cellulose nanofibril-reinforced composites. *Cellulose* **2007**, 14 (5), 419–425.
- (30) Alemdar, A.; Sain, M. Isolation and characterization of nanofibers from agricultural residues Wheat straw and soy hulls. *Bioresour. Technol.* **2008**, 99 (6), 1664–1671.
- (31) Chakraborty, A.; Sain, M.; Kortschot, M. Cellulose microfibrils: A novel method of preparation using high shear refining and cryocrushing. *Holzforschung* **2005**, *59*, 102.
- (32) Johnson, R. K.; Zink-Sharp, A.; Renneckar, S. H.; Glasser, W. G. A new bio-based nanocomposite: fibrillated TEMPO-oxidized celluloses in hydroxypropylcellulose matrix. *Cellulose* **2009**, *16* (2), 227–238.
- (33) Wang, S.; Cheng, Q. A novel process to isolate fibrils from cellulose fibers by high-intensity ultrasonication, Part 1: Process optimization. *J. Appl. Polym. Sci.* **2009**, *113* (2), 1270–1275.
- (34) Frone, A. N.; Panaitescu, D. M.; Donescu, D.; Spataru, C. I.; Radovici, C.; Trusca, R.; Somoghi, R. Preparation and characterization of PVA composites with cellulose nanofibers obtained by unltrasonication. *BioResources* **2011**, *6* (1), 487–512.
- (35) Broder, J. D.; Barrier, J. W.; Lee, K. P.; Bulls, M. M. Biofuels system economics. *World Resour. Rev.* 1995, 7 (4), 560–569.
- (36) Iranmahboob, J.; Nadim, F.; Monemi, S. Optimizing acidhydrolysis: a critical step for production of ethanol from mixed wood chips. *Biomass Bioenergy* **2002**, *22* (5), 401–404.
- (37) Hubbe, M. A.; Rojas, O. J.; Lucia, L. A.; Sain, M. Cellulose nanocomposites: a review. *BioResources* **2008**, 3 (3), 929–980.
- (38) Habibi, Y.; Lucia, L. A.; Rojas, O. J. Cellulose Nanocrystals: Chemistry, Self-Assembly, and Applications. *Chem. Rev.* **2010**, *110* (6), 3479–3500.
- (39) Wang, B.; Sain, M. Isolation of nanofibers from soybean source and their reinforcing capability on synthetic polymers. *Compos. Sci. Technol.* **2007**, *67* (11), 2521–2527.
- (40) Filson, P. B.; Dawson-Andoh, B. E. Sono-chemical preparation of cellulose nanocrystals from lignocellulose derived materials. *Bioresour. Technol.* **2009**, *100* (7), 2259–2264.
- (41) Elazzouzi-Hafraoui, S.; Nishiyama, Y.; Putaux, J.-L.; Heux, L.; Dubreuil, F.; Rochas, C. The Shape and Size Distribution of Crystalline Nanoparticles Prepared by Acid Hydrolysis of Native Cellulose. *Biomacromolecules* **2008**, 9 (1), 57–65.
- (42) Dong, X. M.; Revol, J.-F.; Gray, D. G. Effect of microcrystallite preparation conditions on the formation of colloid crystals of cellulose. *Cellulose* **1998**, *5* (1), 19–32.
- (43) Beck-Candanedo, S.; Roman, M.; Gray, D. G. Effect of Reaction Conditions on the Properties and Behavior of Wood Cellulose Nanocrystal Suspensions. *Biomacromolecules* **2005**, *6* (2), 1048–1054.
- (44) Bondeson, D.; Mathew, A.; Oksman, K. Optimization of the isolation of nanocrystals from microcrystalline celluloseby acid hydrolysis. *Cellulose* **2006**, *13* (2), 171.
- (45) Karim, Z.; Afrin, S.; Husain, Q.; Danish, R. Necessity of enzymatic hydrolysis for production and functionalization of nanocelluloses. *Crit. Rev. Biotechnol.* **2017**, *37* (3), 355–370.
- (46) Henriksson, M.; Henriksson, G.; Berglund, L. A.; Lindström, T. An environmentally friendly method for enzyme-assisted preparation

- of microfibrillated cellulose (MFC) nanofibers. Eur. Polym. J. 2007, 43 (8), 3434-3441.
- (47) Pääkkö, M.; Ankerfors, M.; Kosonen, H.; Nykänen, A.; Ahola, S.; Österberg, M.; Ruokolainen, J.; Laine, J.; Larsson, P. T.; Ikkala, O.; Lindström, T. Enzymatic Hydrolysis Combined with Mechanical Shearing and High-Pressure Homogenization for Nanoscale Cellulose Fibrils and Strong Gels. *Biomacromolecules* **2007**, 8 (6), 1934–1941.
- (48) Tibolla, H.; Pelissari, F. M.; Menegalli, F. C. Cellulose nanofibers produced from banana peel by chemical and enzymatic treatment. *LWT–Food Sci. Technol.* **2014**, *59* (2), 1311–1318.
- (49) Chung, D.; Cha, M.; Snyder, E. N.; Elkins, J. G.; Guss, A. M.; Westpheling, J. Cellulosic ethanol production via consolidated bioprocessing at 75 °C by engineered Caldicellulosiruptor bescii. *Biotechnol. Biofuels* **2015**, *8* (1), 163.
- (50) Yarbrough, J. M.; Zhang, R.; Mittal, A.; Vander Wall, T.; Bomble, Y. J.; Decker, S. R.; Himmel, M. E.; Ciesielski, P. N. Multifunctional Cellulolytic Enzymes Outperform Processive Fungal Cellulases for Coproduction of Nanocellulose and Biofuels. *ACS Nano* **2017**, *11* (3), 3101–3109.
- (51) Camarero Espinosa, S.; Kuhnt, T.; Foster, E. J.; Weder, C. Isolation of Thermally Stable Cellulose Nanocrystals by Phosphoric Acid Hydrolysis. *Biomacromolecules* **2013**, *14* (4), 1223–1230.
- (52) Reid, M. S.; Villalobos, M.; Cranston, E. D. Benchmarking Cellulose Nanocrystals: From the Laboratory to Industrial Production. *Langmuir* **2017**, 33 (7), 1583–1598.
- (53) Battista, O. A. Hydrolysis and Crystallization of Cellulose. *Ind. Eng. Chem.* **1950**, 42 (3), 502–507.
- (54) Lee, S.-Y.; Mohan, D. J.; Kang, I.-A.; Doh, G.-H.; Lee, S.; Han, S. O. Nanocellulose reinforced PVA composite films: Effects of acid treatment and filler loading. *Fibers Polym.* **2009**, *10* (1), 77–82.
- (55) Filpponen, I.; Argyropoulos, D. S. Regular Linking of Cellulose Nanocrystals via Click Chemistry: Synthesis and Formation of Cellulose Nanoplatelet Gels. *Biomacromolecules* **2010**, *11* (4), 1060–1066.
- (56) Liu, D.; Zhong, T.; Chang, P. R.; Li, K.; Wu, Q. Starch composites reinforced by bamboo cellulosic crystals. *Bioresour. Technol.* **2010**, *101* (7), 2529–2536.
- (57) Chen, L.; Ji, T.; Yuan, R.; Mu, L.; Brisbin, L.; Zhu, J. Unveiling Mesopore Evolution in Carbonized Wood: Interfacial Separation, Migration, and Degradation of Lignin Phase. *ACS Sustainable Chem. Eng.* **2015**, 3 (10), 2489–2495.
- (58) Kilzer, F. J.; Broido, A. Speculations on the nature of cellulose pyrolysis. *Pyrodynamics* **1965**, *2*, 151–163.
- (59) Shafizadeh, F.; Bradbury, A. G. W. Thermal degradation of cellulose in air and nitrogen at low temperatures. *J. Appl. Polym. Sci.* 1979, 23 (5), 1431–1442.
- (60) Melo, E.; Kennedy, J. F. Cellulose hydrolysis (biotechnology monographs, Vol. 3) edited by L.-T. Fan, M. M. Gharpuray and Y.-H. Lee, Springer-Verlag, Berlin, Heidelberg, New York, London, Paris and Tokyo, 1987. pp. viii + 198, price DM168.00. ISBN 3-540-17671-3. *Br. Polym. J.* 1988, 20 (6), 532.
- (61) Zwart, R. W. R.; Boerrigter, H.; van der Drift, A. The Impact of Biomass Pretreatment on the Feasibility of Overseas Biomass Conversion to Fischer–Tropsch Products. *Energy Fuels* **2006**, *20* (5), 2192–2197.
- (62) Song, J.; Chen, C.; Zhu, S.; Zhu, M.; Dai, J.; Ray, U.; Li, Y.; Kuang, Y.; Li, Y.; Quispe, N.; Yao, Y.; Gong, A.; Leiste, U. H.; Bruck, H. A.; Zhu, J. Y.; Vellore, A.; Li, H.; Minus, M. L.; Jia, Z.; Martini, A.; Li, T.; Hu, L. Processing bulk natural wood into a high-performance structural material. *Nature* 2018, 554, 224.
- (63) Chen, C.; Song, J.; Zhu, S.; Li, Y.; Kuang, Y.; Wan, J.; Kirsch, D.; Xu, L.; Wang, Y.; Gao, T.; Wang, Y.; Huang, H.; Gan, W.; Gong, A.; Li, T.; Xie, J.; Hu, L. Scalable and Sustainable Approach toward Highly Compressible, Anisotropic, Lamellar Carbon Sponge. *Chem.* 2018, 4 (3), 544–554.
- (64) Trifol, J.; Sillard, C.; Plackett, D.; Szabo, P.; Bras, J.; Daugaard, A. E. Chemically extracted nanocellulose from sisal fibres by a simple and industrially relevant process. *Cellulose* **2017**, 24 (1), 107–118.

- (65) Bhatnagar, A.; Sain, M. Processing of Cellulose Nanofiber-reinforced Composites. *J. Reinf. Plast. Compos.* **2005**, 24 (12), 1259–1268.
- (66) Rånby, B. G. Fibrous macromolecular systems. Cellulose and muscle. The colloidal properties of cellulose micelles. *Discuss. Faraday Soc.* **1951**, *11* (0), 158–164.
- (67) Saito, T.; Nishiyama, Y.; Putaux, J.-L.; Vignon, M.; Isogai, A. Homogeneous Suspensions of Individualized Microfibrils from TEMPO-Catalyzed Oxidation of Native Cellulose. *Biomacromolecules* **2006**, *7* (6), 1687–1691.
- (68) Saito, T.; Hirota, M.; Tamura, N.; Kimura, S.; Fukuzumi, H.; Heux, L.; Isogai, A. Individualization of Nano-Sized Plant Cellulose Fibrils by Direct Surface Carboxylation Using TEMPO Catalyst under Neutral Conditions. *Biomacromolecules* **2009**, *10* (7), 1992–1996.
- (69) Wu, Q.; Henriksson, M.; Liu, X.; Berglund, L. A. A High Strength Nanocomposite Based on Microcrystalline Cellulose and Polyurethane. *Biomacromolecules* **2007**, *8* (12), 3687–3692.
- (70) Galbe, M.; Zacchi, G. Pretreatment of Lignocellulosic Materials for Efficient Bioethanol Production. In *Biofuels*; Olsson, L., Ed.; Springer: Berlin, Heidelberg, 2007; pp 41–65.
- (71) Ballesteros, I.; Negro, M. J.; Oliva, J. M.; Cabañas, A.; Manzanares, P.; Ballesteros, M. Ethanol production from steam-explosion pretreated wheat straw. *Appl. Biochem. Biotechnol.* **2006**, *130* (1), 496–508.
- (72) Okano, K.; Kitagawa, M.; Sasaki, Y.; Watanabe, T. Conversion of Japanese red cedar (Cryptomeria japonica) into a feed for ruminants by white-rot basidiomycetes. *Anim. Feed Sci. Technol.* **2005**, 120 (3), 235–243.
- (73) Lee, J.-W.; Gwak, K. S.; Park, J.-Y.; Park, M.-j.; Choi, D. B.; Kwon, M. H.; Choi, J. W. Biological pretreatment of softwood Pinus densiflora by three white rot fungi. *J. Microbiol.* **2007**, 45 (6), 485–91.
- (74) Hatakka, A. I. Pretreatment of wheat straw by white-rot fungi for enzymic saccharification of cellulose. *Eur. J. Appl. Microbiol. Biotechnol.* **1983**, 18 (6), 350–357.
- (75) Ander, P.; Eriksson, K.-E. Selective Degradation of Wood Components by White-Rot Fungi. *Physiol. Plant.* **1977**, 41 (4), 239–248
- (76) Akin, D. E.; Rigsby, L. L.; Sethuraman, A.; Morrison, W. H., 3rd; Gamble, G. R.; Eriksson, K. E. Alterations in structure, chemistry, and biodegradability of grass lignocellulose treated with the white rot fungi Ceriporiopsis subvermispora and Cyathus stercoreus. *Appl. Environ. Microbiol.* **1995**, *61* (4), 1591–1598.
- (77) Boominathan, K.; Reddy, C. A. cAMP-mediated differential regulation of lignin peroxidase and manganese-dependent peroxidase production in the white-rot basidiomycete Phanerochaete chrysosporium. *Proc. Natl. Acad. Sci. U. S. A.* 1992, 89 (12), 5586.
- (78) Singh, P.; Suman, A.; Tiwari, P.; Arya, N.; Gaur, A.; Shrivastava, A. K. Biological pretreatment of sugarcane trash for its conversion to fermentable sugars. *World J. Microbiol. Biotechnol.* **2008**, 24 (5), 667–673.
- (79) Kumar, A. K.; Sharma, S. Recent updates on different methods of pretreatment of lignocellulosic feedstocks: a review. *Bioresour Bioprocess* **2017**, *4* (1), 7.
- (80) Guan, H.; Cheng, Z.; Wang, X. Highly Compressible Wood Sponges with a Spring-like Lamellar Structure as Effective and Reusable Oil Absorbents. ACS Nano 2018, 12 (10), 10365–10373.
- (81) Fu, Q.; Ansari, F.; Zhou, Q.; Berglund, L. A. Wood Nanotechnology for Strong, Mesoporous, and Hydrophobic Biocomposites for Selective Separation of Oil/Water Mixtures. *ACS Nano* **2018**, 12 (3), 2222–2230.
- (82) Vidiella del Blanco, M.; Fischer, E. J.; Cabane, E. Underwater Superoleophobic Wood Cross Sections for Efficient Oil/Water Separation. *Adv. Mater. Interfaces* **2017**, *4* (21), 1700584.
- (83) Keplinger, T.; Wang, X.; Burgert, I. Nanofibrillated cellulose composites and wood derived scaffolds for functional materials. *J. Mater. Chem. A* **2019**, *7* (7), 2981–2992.
- (84) Qian, X.; Ding, S.-Y.; Nimlos, M. R.; Johnson, D. K.; Himmel, M. E. Atomic and Electronic Structures of Molecular Crystalline

- Cellulose I\(\beta\): A First-Principles Investigation. *Macromolecules* **2005**, 38 (25), 10580–10589.
- (85) Qian, X. The effect of cooperativity on hydrogen bonding interactions in native cellulose I β from ab initio molecular dynamics simulations. *Mol. Simul.* **2008**, 34 (2), 183–191.
- (86) Li, Y.; Lin, M.; Davenport, J. W. Ab Initio Studies of Cellulose I: Crystal Structure, Intermolecular Forces, and Interactions with Water. J. Phys. Chem. C 2011, 115 (23), 11533–11539.
- (87) Ishikawa, T.; Hayakawa, D.; Miyamoto, H.; Ozawa, M.; Ozawa, T.; Ueda, K. Ab initio studies on the structure of and atomic interactions in cellulose IIII crystals. *Carbohydr. Res.* **2015**, 417, 72–77.
- (88) Bučko, T.; Tunega, D.; Ángyán, J. G.; Hafner, J. Ab Initio Study of Structure and Interconversion of Native Cellulose Phases. *J. Phys. Chem. A* **2011**, *115* (35), 10097–10105.
- (89) Mazeau, K.; Heux, L. Molecular dynamics simulations of bulk native crystalline and amorphous structures of cellulose. *J. Phys. Chem. B* **2003**, *107* (10), 2394–2403.
- (90) Mazeau, K.; Rivet, A. Wetting the (110) and (100) Surfaces of $I\beta$ Cellulose Studied by Molecular Dynamics. *Biomacromolecules* **2008**, 9 (4), 1352–1354.
- (91) Matthews, J. F.; Skopec, C. E.; Mason, P. E.; Zuccato, P.; Torget, R. W.; Sugiyama, J.; Himmel, M. E.; Brady, J. W. Computer simulation studies of microcrystalline cellulose *Iβ. Carbohydr. Res.* **2006**, *341* (1), 138–152.
- (92) Matthews, J. F.; Bergenstråhle, M.; Beckham, G. T.; Himmel, M. E.; Nimlos, M. R.; Brady, J. W.; Crowley, M. F. High-Temperature Behavior of Cellulose I. *J. Phys. Chem. B* **2011**, *115* (10), 2155–2166.
- (93) Janesko, B. G. Modeling interactions between lignocellulose and ionic liquids using DFT-D. *Phys. Chem. Chem. Phys.* **2011**, *13* (23), 11393–11401.
- (94) Payal, R. S.; Balasubramanian, S. Dissolution of cellulose in ionic liquids: an ab initio molecular dynamics simulation study. *Phys. Chem. Chem. Phys.* **2014**, *16* (33), 17458–17465.
- (95) Liu, H.; Sale, K. L.; Holmes, B. M.; Simmons, B. A.; Singh, S. Understanding the Interactions of Cellulose with Ionic Liquids: A Molecular Dynamics Study. *J. Phys. Chem. B* **2010**, *114* (12), 4293–4301.
- (96) Zhao, Y. L.; Liu, X. M.; Wang, J. J.; Zhang, S. J. Effects of Cationic Structure on Cellulose Dissolution in Ionic Liquids: A Molecular Dynamics Study. *ChemPhysChem* **2012**, *13* (13), 3126–3133.
- (97) Zhao, Y.; Liu, X.; Wang, J.; Zhang, S. Effects of anionic structure on the dissolution of cellulose in ionic liquids revealed by molecular simulation. *Carbohydr. Polym.* **2013**, *94* (2), 723–730.
- (98) Rabideau, B. D.; Agarwal, A.; Ismail, A. E. Observed Mechanism for the Breakup of Small Bundles of Cellulose I alpha and I beta in Ionic Liquids from Molecular Dynamics Simulations. *J. Phys. Chem. B* **2013**, *117* (13), 3469–3479.
- (99) Bergenstråhle, M.; Berglund, L. A.; Mazeau, K. Thermal Response in Crystalline Iβ Cellulose: A Molecular Dynamics Study. J. Phys. Chem. B **2007**, 111 (30), 9138–9145.
- (100) Assary, R. S.; Curtiss, L. A. Thermochemistry and Reaction Barriers for the Formation of Levoglucosenone from Cellobiose. *ChemCatChem* **2012**, 4 (2), 200–205.
- (101) Mayes, H. B.; Broadbelt, L. J. Unraveling the Reactions that Unravel Cellulose. J. Phys. Chem. A 2012, 116 (26), 7098-7106.
- (102) Agarwal, V.; Dauenhauer, P. J.; Huber, G. W.; Auerbach, S. M. Ab Initio Dynamics of Cellulose Pyrolysis: Nascent Decomposition Pathways at 327 and 600 °C. J. Am. Chem. Soc. 2012, 134 (36), 14958–14972.
- (103) Agarwal, V.; Huber, G. W.; Conner, W. C.; Auerbach, S. M. Simulating infrared spectra and hydrogen bonding in cellulose $I\beta$ at elevated temperatures. *J. Chem. Phys.* **2011**, *135* (13), 134506.
- (104) Beste, A. ReaxFF Study of the Oxidation of Softwood Lignin in View of Carbon Fiber Production. *Energy Fuels* **2014**, 28 (11), 7007–7013.

- (105) Zheng, M.; Wang, Z.; Li, X.; Qiao, X.; Song, W.; Guo, L. Initial reaction mechanisms of cellulose pyrolysis revealed by ReaxFF molecular dynamics. *Fuel* **2016**, *177*, 130–141.
- (106) Paajanen, A.; Vaari, J. High-temperature decomposition of the cellulose molecule: a stochastic molecular dynamics study. *Cellulose* **2017**, 24 (7), 2713–2725.
- (107) Gomes, T. C. F.; Skaf, M. S. Cellulose-Builder: A toolkit for building crystalline structures of cellulose. *J. Comput. Chem.* **2012**, 33 (14), 1338–1346.
- (108) Nishiyama, Y.; Langan, P.; Chanzy, H. Crystal Structure and Hydrogen-Bonding System in Cellulose I β from Synchrotron X-ray and Neutron Fiber Diffraction. *J. Am. Chem. Soc.* **2002**, *124* (31), 9074–9082.
- (109) Chen, C.; Zhao, L.; Wang, J.; Lin, S. Reactive Molecular Dynamics Simulations of Biomass Pyrolysis and Combustion under Various Oxidative and Humidity Environments. *Ind. Eng. Chem. Res.* **2017**, *56* (43), 12276–12288.
- (110) Wu, X.; Moon, R. J.; Martini, A. Tensile strength of $I\beta$ crystalline cellulose predicted by molecular dynamics simulation. *Cellulose* **2014**, 21 (4), 2233–2245.
- (111) van Duin, A. C. T.; Dasgupta, S.; Lorant, F.; Goddard, W. A. ReaxFF: A reactive force field for hydrocarbons. *J. Phys. Chem. A* **2001**, *105* (41), 9396–9409.
- (112) Monti, S.; Corozzi, A.; Fristrup, P.; Joshi, K. L.; Shin, Y. K.; Oelschlaeger, P.; van Duin, A. C. T.; Barone, V. Exploring the conformational and reactive dynamics of biomolecules in solution using an extended version of the glycine reactive force field. *Phys. Chem. Chem. Phys.* **2013**, *15* (36), 15062–15077.
- (113) Zhang, W.; van Duin, A. C. T. Improvement of the ReaxFF Description for Functionalized Hydrocarbon/Water Weak Interactions in the Condensed Phase. *J. Phys. Chem. B* **2018**, *122* (14), 4083–4092.
- (114) Zhang, W.; van Duin, A. C. T. ReaxFF Reactive Molecular Dynamics Simulation of Functionalized Poly(phenylene oxide) Anion Exchange Membrane. *J. Phys. Chem. C* **2015**, *119* (49), 27727–27736.
- (115) Castro-Marcano, F.; Russo, M. F.; van Duin, A. C. T.; Mathews, J. P. Pyrolysis of a large-scale molecular model for Illinois no. 6 coal using the ReaxFF reactive force field. *J. Anal. Appl. Pyrolysis* **2014**, *109*, 79–89.
- (116) Senftle, T. P.; Hong, S.; Islam, M. M.; Kylasa, S. B.; Zheng, Y.; Shin, Y. K.; Junkermeier, C.; Engel-Herbert, R.; Janik, M. J.; Aktulga, H. M.; Verstraelen, T.; Grama, A.; van Duin, A. C. T. The ReaxFF reactive force-field: development, applications and future directions. npj Comput. Mater. 2016, 2, 15011.
- (117) Liang, T.; Shin, Y. K.; Cheng, Y. T.; Yilmaz, D. E.; Vishnu, K. G.; Verners, O.; Zou, C. Y.; Phillpot, S. R.; Sinnott, S. B.; van Duin, A. C. T. Reactive Potentials for Advanced Atomistic Simulations. *Annu. Rev. Mater. Res.* **2013**, *43*, 109–129.
- (118) Li, P.; Merz, K. M. Metal Ion Modeling Using Classical Mechanics. *Chem. Rev.* **2017**, *117* (3), 1564–1686.
- (119) Abell, G. C. Empirical chemical pseudopotential theory of molecular and metallic bonding. *Phys. Rev. B: Condens. Matter Mater. Phys.* **1985**, 31 (10), 6184–6196.
- (120) Tersoff, J. New empirical model for the structural properties of silicon. *Phys. Rev. Lett.* **1986**, 56 (6), 632–635.
- (121) Tersoff, J. New empirical approach for the structure and energy of covalent systems. *Phys. Rev. B: Condens. Matter Mater. Phys.* 1988, 37 (12), 6991–7000.
- (122) Tersoff, J. Empirical Interatomic Potential for Carbon, with Applications to Amorphous Carbon. *Phys. Rev. Lett.* **1988**, *61* (25), 2879–2882.
- (123) Tersoff, J. Modeling solid-state chemistry: Interatomic potentials for multicomponent systems. *Phys. Rev. B: Condens. Matter Mater. Phys.* **1989**, 39 (8), 5566–5568.
- (124) Qiao, Q.; Liu, C.; Gao, W.; Huang, L. Graphene oxide model with desirable structural and chemical properties. *Carbon* **2019**, *143*, 566–577.
- (125) Huang, L.; Seredych, M.; Bandosz, T. J.; Duin, A. C. T. v.; Lu, X.; Gubbins, K. E. Controllable atomistic graphene oxide model and

- its application in hydrogen sulfide removal. J. Chem. Phys. 2013, 139 (19), 194707.
- (126) Zhang, T.; Li, X.; Qiao, X.; Zheng, M.; Guo, L.; Song, W.; Lin, W. Initial Mechanisms for an Overall Behavior of Lignin Pyrolysis through Large-Scale ReaxFF Molecular Dynamics Simulations. *Energy Fuels* **2016**, 30 (4), 3140–3150.
- (127) Zhang, T.; Li, X.; Guo, L. Initial Reactivity of Linkages and Monomer Rings in Lignin Pyrolysis Revealed by ReaxFF Molecular Dynamics. *Langmuir* **2017**, 33 (42), 11646–11657.
- (128) Russo, M. F.; van Duin, A. C. T. Atomistic-scale simulations of chemical reactions: Bridging from quantum chemistry to engineering. *Nucl. Instrum. Methods Phys. Res., Sect. B* **2011**, 269 (14), 1549–1554.
- (129) Mortier, W. J.; Ghosh, S. K.; Shankar, S. Electronegativity equalization method for the calculation of atomic charges in molecules. *J. Am. Chem. Soc.* **1986**, *108* (15), 4315–4320.
- (130) Janssens, G. O. A.; Baekelandt, B. G.; Toufar, H.; Mortier, W. J.; Schoonheydt, R. A. Comparison of cluster and infinite crystal calculations on zeolites with electronegativity equalization method (EEM). *J. Phys. Chem.* **1995**, *99* (10), 3251–3258.
- (131) Agrawalla, S.; van Duin, A. C. T. Development and Application of a ReaxFF Reactive Force Field for Hydrogen Combustion. *J. Phys. Chem. A* **2011**, *115* (6), 960–972.
- (132) Chenoweth, K.; van Duin, A. C. T.; Persson, P.; Cheng, M. J.; Oxgaard, J.; Goddard, W. A. Development and application of a ReaxFF reactive force field for oxidative dehydrogenation on vanadium oxide catalysts. *J. Phys. Chem. C* **2008**, *112* (37), 14645–14654
- (133) Chenoweth, K.; van Duin, A. C. T.; Goddard, W. A. ReaxFF reactive force field for molecular dynamics simulations of hydrocarbon oxidation. *J. Phys. Chem. A* **2008**, *112* (5), 1040–1053.
- (134) Djahedi, C.; Berglund, L. A.; Wohlert, J. Molecular deformation mechanisms in cellulose allomorphs and the role of hydrogen bonds. *Carbohydr. Polym.* **2015**, *130*, 175–182.
- (135) Djahedi, C.; Bergenstråhle-Wohlert, M.; Berglund, L. A.; Wohlert, J. Role of hydrogen bonding in cellulose deformation: the leverage effect analyzed by molecular modeling. *Cellulose* **2016**, 23 (4), 2315–2323.
- (136) Lee, C. M.; Kubicki, J. D.; Fan, B.; Zhong, L.; Jarvis, M. C.; Kim, S. H. Hydrogen-Bonding Network and OH Stretch Vibration of Cellulose: Comparison of Computational Modeling with Polarized IR and SFG Spectra. *J. Phys. Chem. B* **2015**, *119* (49), 15138–15149.
- (137) Araujo, C.; Freire, C. S. R.; Nolasco, M. M.; Ribeiro-Claro, P. J. A.; Rudić, S.; Silvestre, A. J. D.; Vaz, P. D. Hydrogen Bond Dynamics of Cellulose through Inelastic Neutron Scattering Spectroscopy. *Biomacromolecules* **2018**, *19* (4), 1305–1313.
- (138) Altaner, C. M.; Thomas, L. H.; Fernandes, A. N.; Jarvis, M. C. How Cellulose Stretches: Synergism between Covalent and Hydrogen Bonding. *Biomacromolecules* **2014**, *15* (3), 791–798.
- (139) Mercury Mercury User Guide and Tutorials. https://www.ccdc.cam.ac.uk/support-and-resources/CCDCResources/Mercury_UserGuide.pdf (accessed Aug 25, 2019).
- (140) Diamond Diamond, Crystal and Molecular Structure Visualization. https://www.crystalimpact.com/download/diamond/tutorial.pdf (accessed Aug 25, 2019).
- (141) Truesdell, C. The rational mechanics of flexible or elastic bodies, 1638–1788: introduction to Leonhardi Euleri opera omnia vol X et XI seriei secundae. Orell Füssli: Turici, 1960.
- (142) Matsuo, M.; Sawatari, C.; Iwai, Y.; Ozaki, F. Effect of orientation distribution and crystallinity on the measurement by x-ray diffraction of the crystal lattice moduli of cellulose I and II. *Macromolecules* **1990**, 23 (13), 3266–3275.
- (143) Eichhorn, S. J.; Young, R. J.; Davies, G. R. Modeling Crystal and Molecular Deformation in Regenerated Cellulose Fibers. *Biomacromolecules* **2005**, *6* (1), 507–513.
- (144) Tanaka, F.; Iwata, T. Estimation of the Elastic Modulus of Cellulose Crystal by Molecular Mechanics Simulation. *Cellulose* **2006**, 13 (5), 509–517.

- (145) Šturcová, A.; Davies, G. R.; Eichhorn, S. J. Elastic Modulus and Stress-Transfer Properties of Tunicate Cellulose Whiskers. *Biomacromolecules* **2005**, *6* (2), 1055–1061.
- (146) Eichhorn, S. J.; Davies, G. R. Modelling the crystalline deformation of native and regenerated cellulose. *Cellulose* **2006**, *13* (3), 291–307.
- (147) Hossain, D.; Tschopp, M. A.; Ward, D. K.; Bouvard, J. L.; Wang, P.; Horstemeyer, M. F. Molecular dynamics simulations of deformation mechanisms of amorphous polyethylene. *Polymer* **2010**, *51* (25), 6071–6083.
- (148) Plimpton, S. Fast Parallel Algorithms for Short-Range Molecular Dynamics. *J. Comput. Phys.* **1995**, *117* (1), 1–19.
- (149) Spearot, D. E.; Tschopp, M. A.; Jacob, K. I.; McDowell, D. L. Tensile strength of (100) and (110) tilt bicrystal copper interfaces. *Acta Mater.* **2007**, *55* (2), 705–714.
- (150) Tschopp, M. A.; Spearot, D. E.; McDowell, D. L. Atomistic simulations of homogeneous dislocation nucleation in single crystal copper. *Modell. Simul. Mater. Sci. Eng.* **2007**, *15* (7), 693–709.
- (151) Tschopp, M. A.; McDowell, D. L. Influence of single crystal orientation on homogeneous dislocation nucleation under uniaxial loading. *J. Mech. Phys. Solids* **2008**, *56* (5), 1806–1830.
- (152) Mishin, Y.; Farkas, D.; Mehl, M. J.; Papaconstantopoulos, D. A. Interatomic potentials for monoatomic metals from experimental data and ab initio calculations. *Phys. Rev. B: Condens. Matter Mater. Phys.* 1999, 59 (5), 3393–3407.
- (153) Kroon-Batenburg, L. M. J.; Kroon, J. The crystal and molecular structures of cellulose I and II. *Glycoconjugate J.* **1997**, *14* (5), 677–690.
- (154) Viëtor, R. J.; Mazeau, K.; Lakin, M.; Pérez, S. A priori crystal structure prediction of native celluloses. *Biopolymers* **2000**, *54* (5), 342–354.
- (155) Reiling, S.; Brickmann, J. Theoretical investigations on the structure and physical properties of cellulose. *Macromol. Theory Simul.* **1995**, *4* (4), 725–743.
- (156) Wada, M.; Okano, T. Localization of I α and I β phases in algal cellulose revealed by acid treatments. *Cellulose* **2001**, 8 (3), 183–188.
- (157) Popescu, M.-C.; Popescu, C.-M.; Lisa, G.; Sakata, Y. Evaluation of morphological and chemical aspects of different wood species by spectroscopy and thermal methods. *J. Mol. Struct.* **2011**, 988 (1), 65–72.
- (158) Poletto, M.; Ornaghi, L. H.; Zattera, J. A. Native Cellulose: Structure, Characterization and Thermal Properties. *Materials* **2014**, 7 (9), 6105.
- (159) Rismiller, S. C.; Groves, M. M.; Meng, M.; Dong, Y.; Lin, J. Water assisted liquefaction of lignocellulose biomass by ReaxFF based molecular dynamic simulations. *Fuel* **2018**, *215*, 835–843.
- (160) Jahirul, I. M.; Rasul, G. M.; Chowdhury, A. A.; Ashwath, N. Biofuels Production through Biomass Pyrolysis —A Technological Review. *Energies* **2012**, *5* (12), 4952.
- (161) Yui, T.; Nishimura, S.; Akiba, S.; Hayashi, S. Swelling behavior of the cellulose I β crystal models by molecular dynamics. *Carbohydr. Res.* **2006**, 341 (15), 2521–2530.
- (162) van Duin, A. C. T.; Dasgupta, S.; Lorant, F.; Goddard, W. A. ReaxFF: A Reactive Force Field for Hydrocarbons. *J. Phys. Chem. A* **2001**, *105* (41), 9396–9409.
- (163) Zhu, C.; Krumm, C.; Facas, G. G.; Neurock, M.; Dauenhauer, P. J. Energetics of cellulose and cyclodextrin glycosidic bond cleavage. *React. Chem. Eng.* **2017**, 2 (2), 201–214.
- (164) Kimball, J. W. The Energy Relationships in Cellular Respiration and Photosynthesis: the Balance Sheet. https://www.biology-pages.info/B/BalanceSheet.html (accessed Sept 2, 2019).
- (165) Steiner, T. The Hydrogen Bond in the Solid State. *Angew. Chem., Int. Ed.* **2002**, 41 (1), 48–76.
- (166) Diddens, I.; Murphy, B.; Krisch, M.; Müller, M. Anisotropic Elastic Properties of Cellulose Measured Using Inelastic X-ray Scattering. *Macromolecules* **2008**, *41* (24), 9755–9759.
- (167) Nakamae, K.; Nishino, T.; Shimizu, Y.; Matsumoto, T. Experimental Determination of the Elastic Modulus of Crystalline

Regions of Some Aromatic Polyamides, Aromatic Polyesters, and Aromatic Polyether Ketone. *Polym. J.* 1987, 19, 451.

- (168) Sakurada, I.; Nukushina, Y.; Ito, T. Experimental determination of the elastic modulus of crystalline regions in oriented polymers. *J. Polym. Sci.* **1962**, *57* (165), 651–660.
- (169) Moon, R. J.; Martini, A.; Nairn, J.; Simonsen, J.; Youngblood, J. Cellulose nanomaterials review: structure, properties and nanocomposites. *Chem. Soc. Rev.* **2011**, *40* (7), 3941–3994.
- (170) Tashiro, K.; Kobayashi, M. Calculation of crystallite modulus of native cellulose. *Polym. Bull.* **1985**, *14* (3), 213–218.
- (171) Neyertz, S.; Pizzi, A.; Merlin, A.; Maigret, B.; Brown, D.; Deglise, X. A new all-atom force field for crystalline cellulose I. *J. Appl. Polym. Sci.* **2000**, 78 (11), 1939–1946.
- (172) Saito, T.; Kuramae, R.; Wohlert, J.; Berglund, L. A.; Isogai, A. An Ultrastrong Nanofibrillar Biomaterial: The Strength of Single Cellulose Nanofibrils Revealed via Sonication-Induced Fragmentation. *Biomacromolecules* **2013**, *14* (1), 248–253.
- (173) Mark, R. E. Cell wall mechanics of tracheids; Yale University Press: New Haven, CT; London, 1967.